Finite-momentum excitons in rubrene single crystals

Tobias Lettmann* and Michael Rohlfing
Institut für Festkörpertheorie, Westfälische Wilhelms-Universität Münster, 48149 Münster, Germany

(Received 30 June 2021; accepted 15 September 2021; published 23 September 2021)

Excitons with nonzero momenta and their energy dependence are important for time dependent phenomena such as transport properties or the coupling to external or internal fields, for example in electron energy loss spectroscopy. In this paper we calculate the momentum dependent energy landscape of excitons in rubrene single crystals. We show that singlet excitons exhibit a dispersion that is qualitatively similar to the electronic valence and conduction bands, namely a relatively large bandwidth along Γ–Y and much flatter bands along Γ–X and Γ–Z. However, the absolute value of the bandwidths is significantly weaker than for both electronic bands. Triplet excitons, on the other hand, show much less dispersion and the exciton bands are much flatter than their singlet counterparts.

DOI: 10.1103/PhysRevB.104.115427

I. INTRODUCTION

Single crystals of rubrene ((5,6,11,12)-tetraphenyltetracene) have received much attention for their remarkable charge transport properties. The hole mobility of up to 40 $cm^2/V\,s$ is one of the highest among organic systems [1]. Another interesting feature is the anisotropy of the charge transport, which is much higher along the direction of the close stacking of the molecules than along the two orthogonal directions [2–4]. This is thought to be a consequence of bandlike carrier transport (as opposed to molecular hopping) as suggested by various experiments [5–7].

Experimental measurements [8,9] and theoretical calculations [10,11] of the electronic band structure show the same anisotropic behavior. Along the close-stacked direction (Γ–Y) a large bandwidth/dispersion is found, whereas the bands along the other directions are much flatter.

However, if rubrene single crystals are to be used in organic optoelectronic devices such as light emitting diodes or organic solar cells, as is proposed and investigated by various studies [12–16], the properties of excitons are also relevant. While the optical absorption energies have been determined theoretically [17] as well as experimentally [11,18,19], we are not aware of any theoretical investigations of the finite-momentum landscape for the excitons. This landscape may be relevant in determining the exciton transport properties, which are important design criteria for optoelectronic devices, and can for example be measured by electron energy loss spectroscopy.

Similar to the electrons and holes in the electronic band structure excitons can also be classified according to their total momentum (which relates to their center-of-mass motion) into an exciton band structure. In this paper we calculate the momentum dependence of the exciton energies in order to determine whether there is a similar anisotropy as in the electronic band structure or if the electron-hole interaction leads to a different behavior.

Our calculations use the GW/Bethe-Salpeter equation (BSE) framework of many-body perturbation theory which has become one of the standard procedures for the calculation of optical properties of extended (molecular) crystals [20,21] as well as molecules and polymers [22–26]. Recently it also has increasingly been used for the calculation of finite-momentum excitons [27–31].

Within GW/BSE an excitonic state $|S,\mathbf{Q}\rangle$ with exciton momentum $\mathbf{Q}$ is a linear combination of all possible transitions between occupied valence states $|v,\mathbf{k}\rangle$ and unoccupied conduction bands $|c,\mathbf{k}'\rangle$ whose momenta differ by $\mathbf{Q}$. It can therefore be expressed as

$$|S,\mathbf{Q}\rangle = \sum_{v}^{\text{occ}} \sum_{c}^{\text{empty}} \sum_{\mathbf{k}} \left(A^{S,\mathbf{Q}}_{vc,\mathbf{k}} \, |v,\mathbf{k} \rightarrow c,(\mathbf{k}+\mathbf{Q})\rangle + B^{S,\mathbf{Q}}_{vc,\mathbf{k}} \, |v,(\mathbf{k}+\mathbf{Q}) \leftarrow c,\mathbf{k}\rangle \right). \tag{1}$$

Here resonant transitions (excitations) are accompanied by coefficients $A^{S,\mathbf{Q}}_{vc,\mathbf{k}}$ and antiresonant transitions (de-excitations) by coefficients $B^{S,\mathbf{Q}}_{vc,\mathbf{k}}$. The exciton energies can then be obtained by solving the BSE

$$\begin{pmatrix} D_A + K^{\mathrm{d}}_{AA} + 2K^{\mathrm{x}}_{AA} & K^{\mathrm{d}}_{AB} + 2K^{\mathrm{x}}_{AB} \\ K^{\mathrm{d}}_{BA} + 2K^{\mathrm{x}}_{BA} & D_B + K^{\mathrm{d}}_{BB} + 2K^{\mathrm{x}}_{BB} \end{pmatrix} \begin{pmatrix} A^S \\ B^S \end{pmatrix} = \Omega_S \begin{pmatrix} A^S \\ -B^S \end{pmatrix} \tag{2}$$

for singlet excitations and

$$\begin{pmatrix} D_A + K^{\mathrm{d}}_{AA} & K^{\mathrm{d}}_{AB} \\ K^{\mathrm{d}}_{BA} & D_B + K^{\mathrm{d}}_{BB} \end{pmatrix} \begin{pmatrix} A^S \\ B^S \end{pmatrix} = \Omega_S \begin{pmatrix} A^S \\ -B^S \end{pmatrix} \tag{3}$$

for triplet excitations. These equations have to be solved separately for each individual exciton momentum.

In Eqs. (2) and (3) the diagonal matrices D contain the quasiparticle energy differences of the relevant transitions,

*t.lettmann@uni-muenster.de

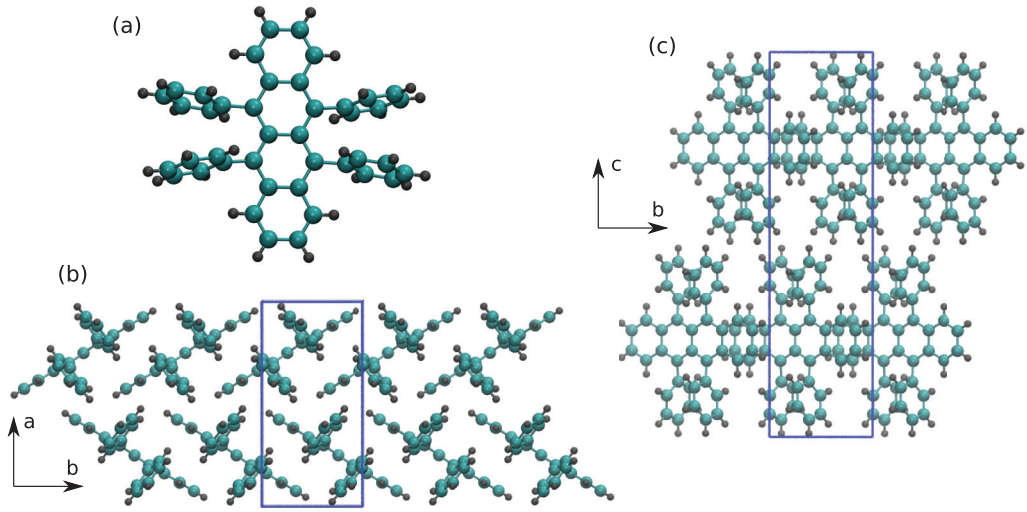

FIG. 1. Atomic structure of rubrene single crystals. (a) isolated molecule, (b) view of the crystal along the c axis showing the herringbone-like arrangement, and (c) view of the crystal along the a axis showing the two separated ab planes. For better visibility the second ab plane is not shown in (b). Carbon atoms are shown in cyan and hydrogen atoms in gray. The unit cell is drawn in blue.

i.e., $E^{\mathrm{QP}}_{c,\mathbf{k}+\mathbf{Q}} - E^{\mathrm{QP}}_{v,\mathbf{k}}$ for D_A and $E^{\mathrm{QP}}_{c,\mathbf{k}} - E^{\mathrm{QP}}_{v,\mathbf{k}+\mathbf{Q}}$ for D_B. K^{d} and K^{x} represent the direct and exchange part of the electron-hole interaction, respectively. They are for the resonant-resonant part given by

$$K^{\mathrm{d},AA}_{vc\mathbf{k},v'c'\mathbf{k}'} = -\int d\mathbf{x}d\mathbf{x}'\, \psi^*_{c,\mathbf{k}+\mathbf{Q}}(\mathbf{x})\psi_{c',\mathbf{k}'+\mathbf{Q}}(\mathbf{x})W(\mathbf{r},\mathbf{r}') \times \psi_{v,\mathbf{k}}(\mathbf{x}')\psi^*_{v',\mathbf{k}'}(\mathbf{x}') \tag{4}$$

and

$$K^{\mathrm{x},AA}_{vc\mathbf{k},v'c'\mathbf{k}'} = \int d\mathbf{x}d\mathbf{x}'\, \psi_{v,\mathbf{k}}(\mathbf{x})\psi^*_{c,\mathbf{k}+\mathbf{Q}}(\mathbf{x})v(\mathbf{r},\mathbf{r}') \times \psi^*_{v',\mathbf{k}'}(\mathbf{x}')\psi_{c',\mathbf{k}'+\mathbf{Q}}(\mathbf{x}'). \tag{5}$$

Here v and W represent the bare and screened Coulomb interaction, respectively. The screened interaction W is obtained as $W = \varepsilon^{-1}v$, i.e., via the convolution of the inverse dielectric function $\varepsilon^{-1}(\mathbf{r},\mathbf{r}',\omega)$ and the bare Coulomb interaction. The dielectric function describes all dielectric polarizability mechanisms within the system. Each ψ in Eqs. (4) and (5) denotes the indicated quasiparticle wave function. For the interaction matrices involving antiresonant transitions (B) the corresponding indices v' and c' have to be switched on the right-hand side of each equation.

More detailed discussions of this formalism can be found in Refs. [32,33].

An often used approximation is the Tamm-Dancoff approximation (TDA) that neglects the resonant-antiresonant coupling ($K_{AB} = K_{BA} = 0$) and thereby decouples the excitations and de-excitations. However, it has been shown numerous times that this is problematic for singlet excitons in small organic molecules [33–38]. As rubrene molecules should be considered small for this purpose, we will use the full BSE in addition to the simpler TDA calculations throughout this work.

II. COMPUTATIONAL DETAILS

Rubrene crystallizes in an orthorhombic unit cell containing four molecules arranged in a herringbonelike structure. Depictions of this arrangement can be seen in Fig. 1. Within the unit cell the four molecules are arranged in two herringbone-like ab planes of two molecules each. The planes are separated by $c/2$ and shifted slightly in the b direction [see Fig. 1(c)]. This results in closely stacked molecules in the b direction, whereas the molecules are further apart in the a and c directions.

In this work we use the experimental structure measured by Jurchescu *et al.* via x-ray diffraction (Ref. [39]) without any theoretical optimizations. They obtained lattice constants of $a = 14.433$ Å, $b = 7.193$ Å, and $c = 26.86$ Å at a temperature of 293 K.

In addition to the bulk crystal, we also calculated thin films of rubrene single crystals. For this we chose a slab of two ab planes (i.e., one unit cell, 26.86 Å-thick) with 100 Å vacuum added in the c direction.

Our density functional theory (DFT) calculations, which are used as a starting point for the GW/BSE calculations, were carried out with the local density approximation (LDA) functional and norm-conserving Hamann pseudopotentials [40] in the Kleinman-Bylander form [41]. The basis set consisted of atom-centered gaussians [42] with three decay constants per atom each up to angular momentum $l = 2$, i.e., 30 basis functions per atom. The decay constants were $\alpha = [0.13, 0.78, 3.60]\, a_B^{-2}$ for hydrogen atoms and $\alpha = [0.26, 0.89, 3.48]\, a_B^{-2}$ for carbon atoms. The Brillouin zone was sampled by a grid of $2 \times 4 \times 2$ $\mathbf{k}$ points determined by the scheme developed by Monkhorst and Pack [43].

Tests with varying decay constants and also larger basis sets of 40 functions per atom revealed changes in the Kohn-Sham energies, band gaps, and bandwidths of just 5 meV at most. Changing the $\mathbf{k}$-point grid to a sparser $1 \times 2 \times 1$ or a denser $4 \times 8 \times 4$ grid has virtually no effect on the DFT

results. As the Kohn-Sham energies are anyways corrected by the later GW calculations this seems to be an adequate setup.

In our GW/BSE calculations the dielectric function ε is calculated via the random-phase approximation (RPA) and then described by a generalized plasmon-pole model. The plasmon-pole model is in the form originally introduced by von der Linden and Horsch [44,45]. Its parameters are determined by two independent calculations of the dielectric matrix at $\omega = 0$ and on the imaginary axis at $\omega = i$ Ry.

Although in principle the self-energy Σ would have to be calculated iteratively this is unfeasible. Instead, we calculate the Green functions G and the screened Coulomb interaction W only once from the DFT results. This approach is also known as G_0W_0.

When calculating the self-energy, we use an additional Gaussian basis set to represent the occurring two-point quantities, such as ε or W, as matrices in this basis [45]. This corresponds to density-fitting resolution-of-identity techniques. We use the same decay constants as for the DFT basis set but with functions up to $l = 3$ for the two larger decay constants, which results in 50 basis functions per atom for the auxiliary GWA basis. We also tested other setups for the decay constants, but this produced only minor changes in the results.

The **k**-point sampling for the RPA and the calculation of Σ was also done by a $2 \times 4 \times 2$ grid. The sum over states required for the calculation of ε and Σ is taken over the first 2000 (spin-degenerated) states available from the DFT.

For the BSE calculations the electron-hole interaction was calculated on a $3 \times 7 \times 1$ **k**-point grid, which included the Γ point (where the closest quasiparticle gap is located). The active space for the transitions included in the BSE consisted of 60 valence bands and 100 conduction bands at each point of the grid.

With these parameters the quasiparticle band gap at Γ is converged within 0.05 eV and the bandwidths of the highest valence and lowest conduction bands are converged within 0.01 eV. With those GW results the exciton energies are converged within 0.01 eV.

Further technical details can be found in Refs. [32–34,45,46].

III. ELECTRONIC BAND STRUCTURE

Our result for the electronic band structure along the path Z–Γ–Y–X–Γ is shown in Fig. 2. Overall, our result agrees with previous calculations [10,17,47] and experimental measurements [8,9] in having a relatively large bandwidth along Γ–Y (which corresponds to the b direction in real space), a small bandwidth along Γ–X (a direction), and virtually flat bands along Γ–Z (c direction). For the comparison with our exciton energies (see Sec. IV), the different bandwidths and the quasiparticle gap are listed in Table I.

In general our bandwidths roughly agree with those calculated in Ref. [10] (for both DFT and GWA), although they are up to 0.06 eV larger along Γ–Y. Experimentally (angle-resolved photoelectron spectroscopy) the bandwidth of the valence band along Γ–Y was determined as (larger than) 0.4 eV [8,9], compared to our calculated value of 0.55 eV. Our band gap of 2.6 eV is within the range of previously calculated values. A model geometry with just two molecules per unit cell yielded a band gap of 2.8 eV [17], whereas theoretically optimized structures gave rise to band gaps of 2.5 eV [47] and 2.34 eV [10]. The latter study also took the van der Waals interaction into account.

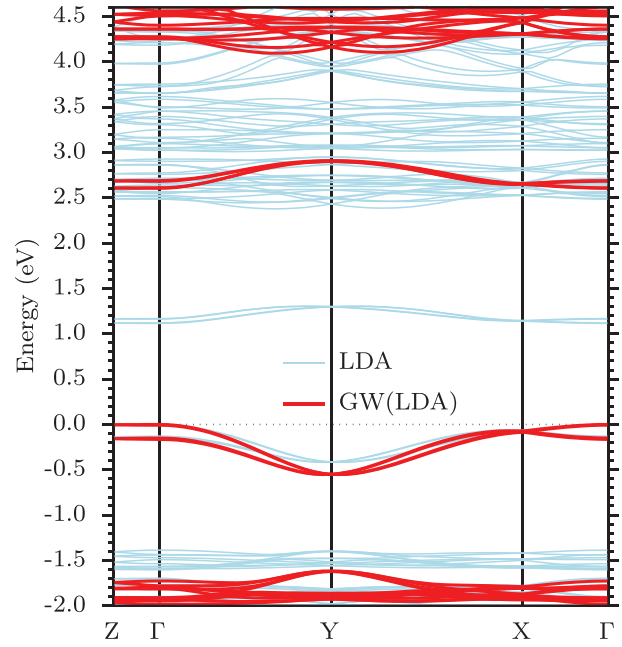

FIG. 2. Electronic band structure within LDA and GWA along Z–Γ–Y–X–Γ. The two band structures are aligned at the valence band maximum at Γ which is set to zero energy. The band structure has a large bandwidth along Γ–Y for the highest valence and lowest conduction bands. The bandwidths along Γ–X and especially Γ–Z are much smaller.

All in all, our band structure therefore agrees with those previously reported. This should provide a reliable basis for our subsequent BSE calculations. The remaining (small) differences are probably due to the different atomic structures and a slightly different theoretical treatment.

The band structure of the thin film is very similar to that of the bulk crystal. The only difference (apart from the missing Γ–Z direction) is a larger quasiparticle band gap of about 3.0 eV. The bandwidths of the bands near the band gap are unchanged compared to the bulk crystal.

TABLE I. The bandwidths W of the highest valence band (VB) and the lowest conduction band (CB) along the Γ–Y and Γ–X directions for LDA and GWA. The band gap at Γ is also listed. All values are given in eV.

	LDA	GWA
$W_{\mathrm{VB}}(\Gamma\text{–Y})$	0.41	0.55
$W_{\mathrm{CB}}(\Gamma\text{–Y})$	0.18	0.30
$W_{\mathrm{VB}}(\Gamma\text{–X})$	0.06	0.07
$W_{\mathrm{CB}}(\Gamma\text{–X})$	0.03	0.04
$E_{\mathrm{Gap}}(\Gamma)$	1.11	2.60

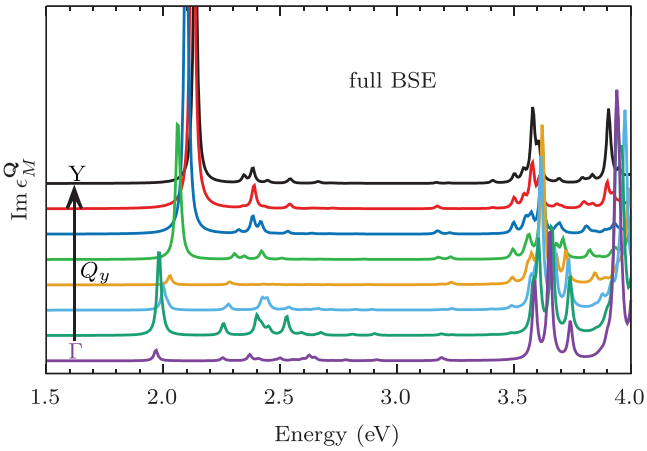

FIG. 3. Imaginary parts of the macroscopic dielectric function of bulk rubrene single crystals for different exciton momenta. The momenta are in Q_y direction and range from zero momentum ($\mathbf{Q} = \Gamma$) to momenta spanning half the Brillouin zone ($\mathbf{Q} = \mathrm{Y}$). For these calculations the full BSE without the TDA was used. The lowest exciton energy increases with increasing exciton momentum.

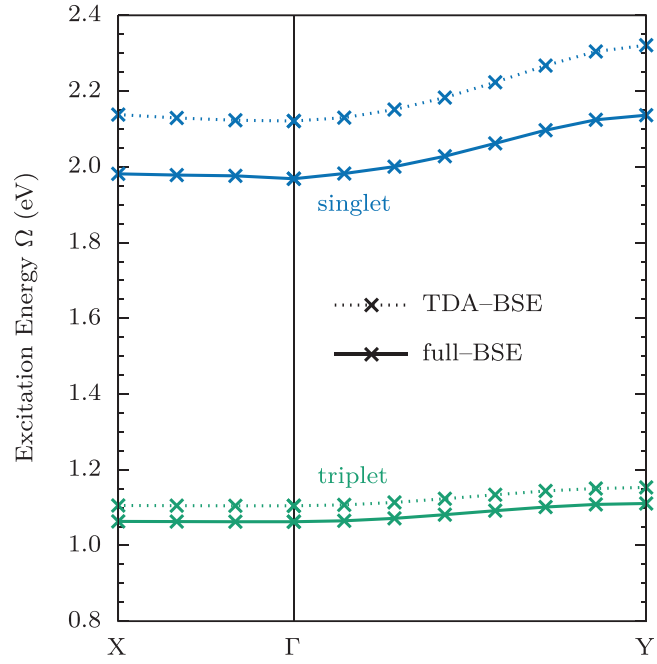

FIG. 4. Plot of the band structure of singlet and triplet excitons of bulk rubrene single crystals along X–Γ–Y. The results of the full BSE are shown with solid lines and those for the TDA-BSE with dotted lines. The dispersion of the triplet energies is much lower than that of the singlet energies.

IV. FINITE-MOMENTUM EXCITONS

A. Bulk crystal

Figure 3 shows the imaginary parts of the macroscopic dielectric function ($\mathrm{Im}\,\epsilon_M^{\mathbf{Q}}$) for different exciton momenta $\mathbf{Q}$ in the Q_y direction, i.e., parallel to Γ–Y. For zero exciton momentum (denoted as $\mathbf{Q} = \Gamma$ in Fig. 3) this corresponds to the optical absorption spectrum.

The macroscopic dielectric functions are calculated as a sum of δ peaks located at the exciton energies Ω_S [32]

$$\mathrm{Im}\,\epsilon_M^{\mathbf{Q}}(\omega) = \frac{16\pi e^2}{\omega^2} \sum_S |\mathbf{E} \cdot \langle 0|\mathbf{v}|S, \mathbf{Q}\rangle|^2 \delta(\omega - \Omega_S), \quad (6)$$

where $\mathbf{E}$ is the normalized polarization vector of the light field (We use unpolarized light, i.e., an average over all three cartesian directions). $\mathbf{v}$ is the single-particle velocity operator. The transition matrix element can be expanded in terms of the exciton state [see Eq. (1)] and is given by

$$\langle 0|\mathbf{v}|S, \mathbf{Q}\rangle = \sum_{vc\mathbf{k}} \left(A_{vc\mathbf{k}}^{S,\mathbf{Q}} \langle v, \mathbf{k}|\mathbf{v}|c, \mathbf{k}+\mathbf{Q}\rangle + B_{vc\mathbf{k}}^{S,\mathbf{Q}} \langle c, \mathbf{k}|\mathbf{v}|v, \mathbf{k}+\mathbf{Q}\rangle\right). \quad (7)$$

For better visibility the functions in Fig. 3 were drawn with artificially broadened Lorentz peaks instead of the δ peaks in Eq. (6).

From Fig. 3 it is already apparent that the lowest exciton energy increases as the exciton momentum increases. Fig. 4 then shows the lowest exciton energies in a band structurelike plot that also includes momenta in Q_x direction. Additionally Fig. 4 also includes the energy of the lowest triplet exciton as well as the energies resulting from calculations using the TDA. The triplet energies do not contribute to the dielectric functions shown in Fig. 3 due to the selection rules (they are spin forbidden).

First of all, we obtain an optical absorption energy (at the Γ point, i.e., $\mathbf{Q} = 0$) of 2.12 eV for the TDA and 1.97 eV for the full BSE. This is in reasonably good agreement with experimental values, which range from 2.35 eV [18] via 2.2 eV [11,19] down to 2.04 eV [19]. The remaining discrepancies are a result of the limitations of the mathematical approach, which usually result in slightly lower theoretical exciton energies. Our value is lower than a previously calculated absorption energy of 2.32 eV [17], which was obtained within the TDA. But the difference to our value is solely a result of the higher quasiparticle gap (2.8 eV compared to our band gap of 2.6 eV.) due to the use of a model geometry (see Sec. III). The exciton binding energies obtained in Ref. [17] agree with our values.

Fig. 4 shows that for the singlet excitons employing the TDA leads to energies that are roughly 0.2 eV larger than for the full BSE. This is in the expected range for organic molecules of this size [33,34]. The triplet energies are, as usual, much less affected by the TDA. For them the difference is only about 0.06 eV.

The dispersion of the singlet exciton energies is qualitatively similar to the valence and conduction bands of the electronic band structure. Quantitatively, however, the dispersion is significantly weaker than for both electronic bands. The bandwidths are about 0.2 eV along Γ–Y (roughly two thirds of the bandwidth of the conduction band) and less than 0.02 eV along Γ–X. In contrast the triplet energies show much less dispersion. Here the bandwidth along Γ–Y is only about 0.05 eV and along Γ–X the bands are virtually flat. The concrete values for the bandwidths of both types of excitons are listed in Table II.

All excitons (singlets and triplets) whose energies are depicted in Fig. 4 are mainly composed of transitions from

TABLE II. The bandwidths W of the lowest energy singlet and triplet excitons of bulk rubrene single crystals along the Γ–Y and Γ–X directions calculated with and without the Tamm-Dancoff approximation. For reference the absolute energy at Γ is also listed. All energy values are given in eV.

	TDA-BSE	full BSE
W_{sing}(Γ–Y)	0.20	0.17
W_{trip}(Γ–Y)	0.05	0.05
W_{sing}(Γ–X)	0.02	0.01
W_{trip}(Γ–X)	0.001	0.001
E_{sing}(Γ)	2.12	1.97
E_{trip}(Γ)	1.10	1.06

the highest valence bands into the lowest conduction bands (and vice versa for the full BSE). However, the singlet and triplet excitons differ in their contributions from the different **k** points in the Brillouin zone and the spatial extent of the wave function in real space, which explains the differences in the dispersion/bandwidths.

For the singlet excitons Fig. 5 shows as an example the probability density of the electron for a fixed hole position as well as the contributions from the different **k** points for a relatively large exciton momentum near Y. The **k**-point distribution on the right shows that singlet excitons mainly consist of transitions that start (or end for the full BSE) from (on) the valence band at or near Γ. For zero exciton momentum (not shown here) the highest contribution would be directly at Γ and symmetric around it. For larger exciton momenta, as in Fig. 5, the distribution shifts slightly to $k_y \neq 0$ and is no longer symmetric because the direction of the exciton momentum breaks the spatial symmetry.

This means that the highest contributing transitions all enter with very similar quasiparticle gaps into the BSE. As the exciton momentum changes these quasi-particle gaps follow the dispersion of the conduction band, which consequently leads to the large exciton dispersion along Γ–Y and the small exciton dispersion along Γ–X depicted in Fig. 4. Since the quasiparticle gap for transitions that start at $k_y \neq 0$ is always smaller than that for those starting at $k_y = 0$, this should lead to a reduced bandwidth compared to the conduction band (compare Tables I and II).

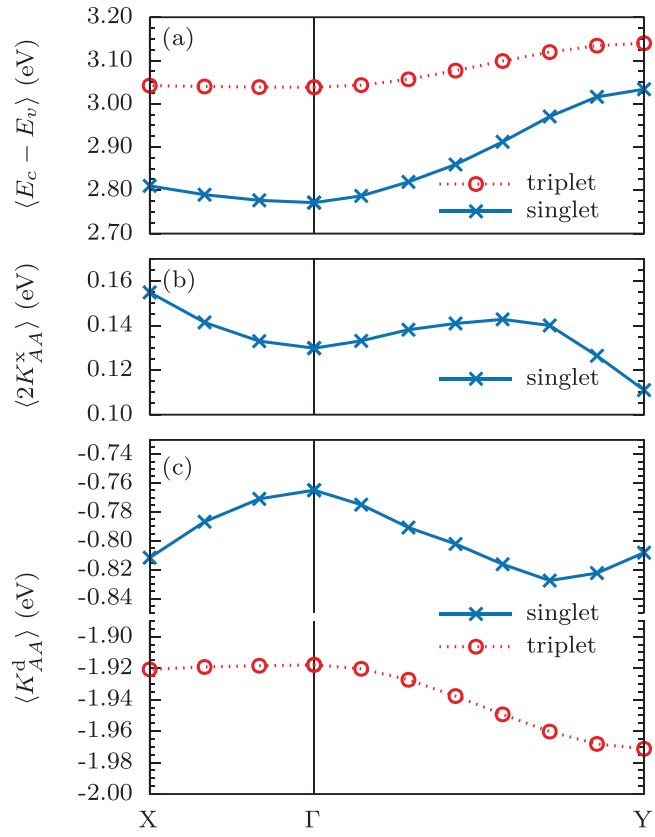

FIG. 6. Expectation values of the different elements of the BSE for the investigated singlet and triplet excitons within the TDA as functions of the exciton momentum **Q**. (a) Expectation value of the quasiparticle gap $E^{\text{QP}}_{c,\mathbf{k}+\mathbf{Q}} - E^{\text{QP}}_{v,\mathbf{k}}$, (b) expectation value of the exchange electron-hole interaction (only singlet) and (c) of the direct electron-hole interaction. Note the different scale of the energy axis in the different subfigures and the break in the energy axis of the direct interaction in (c).

To investigate this in more detail Fig. 6 shows the expectation values of the quasiparticle gap and the two parts of the electron-hole interaction for the different excitons as functions of the exciton momentum **Q**. As just discussed, the expectation value of the quasi-particle gap is qualitatively

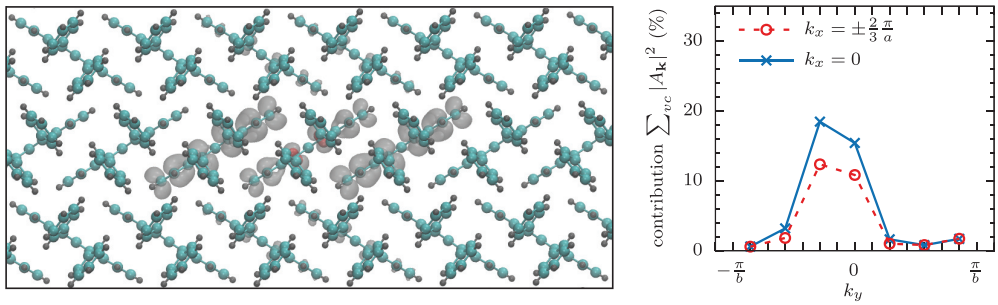

FIG. 5. Left: Probability density $|\chi(\mathbf{x}, \mathbf{x}_h)|^2$ for a singlet exciton with a total momentum near Y, calculated within the Tamm-Dancoff approximation. The hole was fixed at $\mathbf{x}_h$ on the center molecule as indicated by the red dots (these correspond to density maxima of the valence band). The volume enclosed by the indicated isosurface contains 64 % of the probability. Right: Contributions of the different **k** points of the $3 \times 7 \times 1$ grid to the same exciton wave function. The contributions are symmetric around $k_x = 0$ due to symmetry. With respect to k_y the symmetry is broken due to the nonzero exciton momentum.

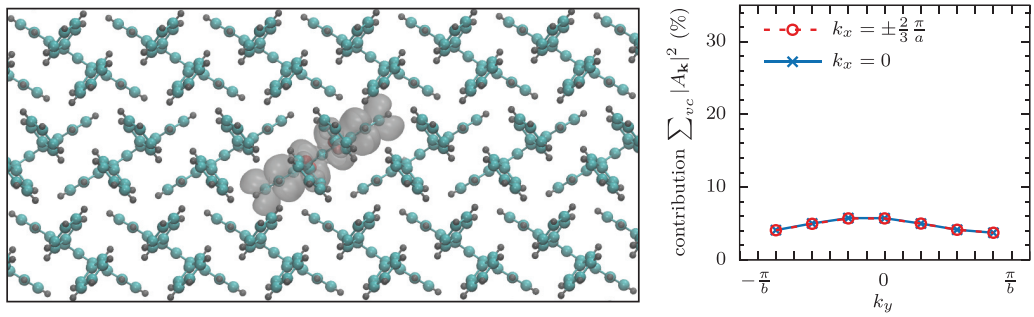

FIG. 7. Left: Probability density $|\chi(\mathbf{x}, \mathbf{x}_h)|^2$ for a triplet exciton with a total momentum near Y, calculated within the Tamm-Dancoff approximation. The hole was fixed at $\mathbf{x}_h$ on the center molecule as indicated by the red dots (these correspond to density maxima of the valence band). The volume enclosed by the indicated isosurface contains 92 % of the probability. Right: Contributions of the different $\mathbf{k}$ points of the $3 \times 7 \times 1$ grid to the same exciton wave function. The contributions are symmetric around $k_x = 0$ due to symmetry. With respect to k_y the symmetry is broken due to the nonzero exciton momentum.

similar to the conduction band, but has a reduced bandwidth of just over 0.2 eV. Note that due to the $\mathbf{k}$ dependence of $A^{S,\mathbf{Q}}_{vc,\mathbf{k}}$, gaps at various $\mathbf{k}$ contribute to this expectation value with different weights $|A^{S,\mathbf{Q}}_{vc,\mathbf{k}}|^2$.

Figure 6 also shows that the variations of the expectation values of the electron-hole interaction for different momenta are an order of magnitude smaller than for the quasiparticle gaps. These variations further reduce the exciton bandwidth as they generally result in a more attractive electron-hole interaction for larger exciton momenta. While the expectation values of the exchange interaction are generally more repulsive for increasing momenta (except for the largest momenta in Γ–Y direction), this is counteracted by the direct interaction, which gets more attractive by even larger amounts (note the different energy scales).

In addition to the $\mathbf{k}$-point distribution, Fig. 5 also shows an exemplary real space probability density for the singlet exciton. This density is widely spread over multiple molecules and is very similar irrespective of the exciton momentum as a result of the very small variations of the electron-hole interaction (see Fig. 6). The probability to find the electron on the same molecule as the hole is about 17 % for all exciton momenta. Finding the electron on the two nearest neighbors in the b direction (horizontal in Fig. 5) has a probability of 42 % for zero exciton momentum. For larger exciton momenta the probability increases up to about 64 %. For the second nearest neighbors in the b direction the probability ranges from 6 % to 1 % and for the neighbors in the a direction (vertical in Fig. 5) the probability is between 20 % and 12 %. Overall, the general magnitude of these probabilities agrees with previously reported ones for zero exciton momentum [17]. The concrete values differ, probably due to a different definition of what constitutes "on a molecule" (within 2 Å of an atom of said molecule in our case). The more compact densities for larger momenta are in line with the slightly more attractive electron-hole interaction observed in Fig. 6.

The triplet excitons on the other hand are very different, as is apparent from the distributions in Fig. 7. The probability density on the left shows a much larger probability to find the electron on the same molecule as the hole than for the singlets. In fact this probability is over 90% in all cases (Previously reported results for zero exciton momentum show a similar distribution [17]). This is a consequence of the missing repulsive exchange interaction and an increased direct electron-hole interaction that leads to the lower overall excitation energy.

Within $\mathbf{k}$ space this distribution means that all $\mathbf{k}$ points contribute roughly equally to the electron-hole amplitude (wave function). See also the right plot in Fig. 7. Because the different transitions start at different points in the Brillouin zone, they are associated with different quasiparticle gaps that enter into the BSE. These quasiparticle gaps react/change differently when the exciton momentum changes. For transitions starting near Γ the gap increases as the exciton momentum increases (as already discussed for the singlet excitons). Transitions starting at k_y near the edge of the Brillouin zone (near Y), on the other hand, are associated with a quasiparticle gap that decreases if the exciton momentum increases from zero. Together these changes partly counteract each other, so that the average quasiparticle gap of the triplet excitons has a much smaller dispersion. This dispersion is then further reduced by the increasing (in absolute terms) electron-hole interaction. Both of these effects can be seen in the expectation values in Fig. 6. Together these effects then result in the much flatter triplet bands in Fig. 4.

B. Thin films

The thin film geometry consisted of to ab planes of molecules and 100 Å of vacuum along the c direction (see Sec. II). For this geometry Fig. 8 shows the imaginary parts of the macroscopic dielectric function for the same momenta as for the bulk crystal in Fig. 3. Figure 9 then shows the corresponding band structure of the lowest energy excitons.

At first glance it is obvious that the momentum dependence of the exciton energies is similar to that of the bulk crystal. Furthermore the concrete exciton energies differ by only up to about 0.05 eV from the bulk crystal. For the bandwidths the difference is even smaller (see the values listed in Table III). This is remarkable because the quasiparticle gap of the electronic band structure of the thin film is about 0.4 eV larger than for the bulk crystal. The electron-hole interaction must therefore be larger by a similar amount. Reasons for this include a reduced screening due to the missing three-dimensional environment and due to the geometric

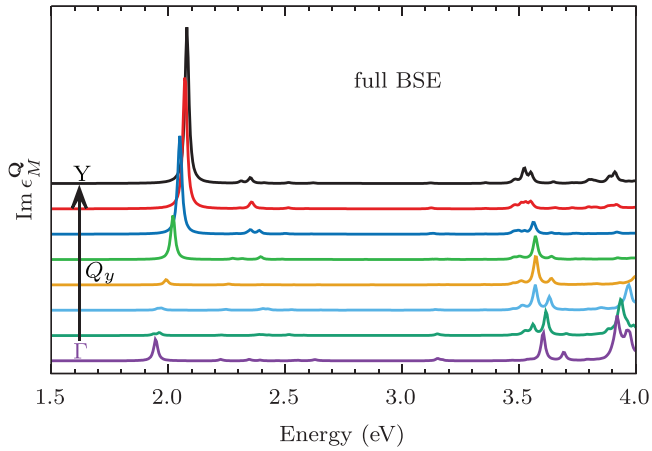

FIG. 8. Imaginary parts of the macroscopic dielectric function of rubrene thin films for different exciton momenta. The momenta are in the Q_y direction and range from no momentum ($\mathbf{Q} = \Gamma$) to momenta spanning half the Brillouin zone ($\mathbf{Q} = \mathrm{Y}$). For these calculations the full BSE without the TDA was used. The lowest exciton energy again increases with increasing exciton momentum.

confinement of the wave functions to just two *ab* planes of molecules.

It is commonly observed in nanostructured systems that increased environmental polarizability (due to adsorbates, substrates, additional layers, etc.) reduces both the fundamental band gap and the electron-hole interaction, largely compensating each other such that exciton energies change very little [48–51]. Removing layers (as in this study) has the opposite effect (increased gap, increased excitonic binding, but similar exciton energies), as observed here.

Although not shown here in detail, the real space probability densities and **k**-point distributions of the thin film excitons do not significantly differ from the bulk ones shown in Fig. 5 and Fig. 7.

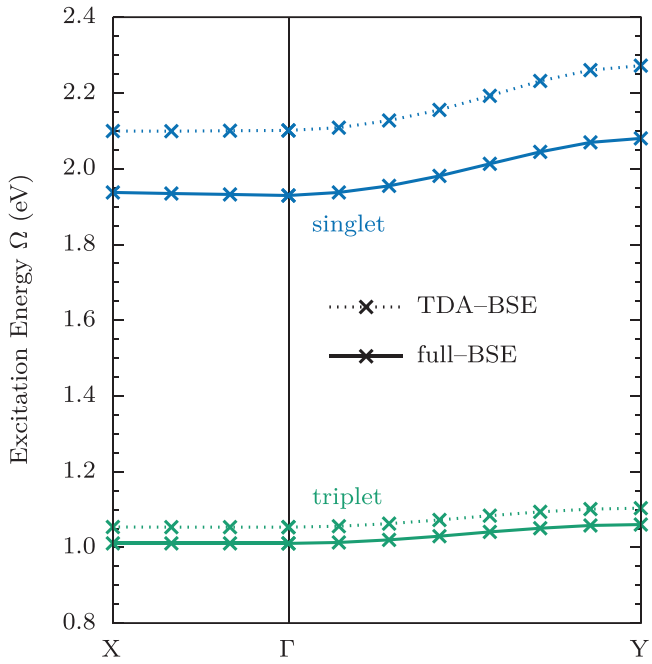

FIG. 9. Plot of the band structure of singlet and triplet excitons of rubrene thin films along X–Γ–Y. The results of the full BSE are shown with solid lines and those for the TDA-BSE with dotted lines. Again, the dispersion of the triplet energies is much lower than that of the singlet energies. The overall energies are similar to those of the bulk crystal.

TABLE III. The bandwidths W of the lowest energy singlet and triplet excitons of rubrene thin films along the Γ–Y and Γ–X directions calculated with and without the TDA. For reference the absolute energy at Γ is also listed. All energy values are given in eV.

	TDA-BSE	Full BSE
$W_{\mathrm{sing}}(\Gamma\text{–Y})$	0.17	0.15
$W_{\mathrm{trip}}(\Gamma\text{–Y})$	0.05	0.05
$W_{\mathrm{sing}}(\Gamma\text{–X})$	0.002	0.01
$W_{\mathrm{trip}}(\Gamma\text{–X})$	0.000	0.000
$E_{\mathrm{sing}}(\Gamma)$	2.10	1.93
$E_{\mathrm{trip}}(\Gamma)$	1.05	1.01

V. CONCLUSIONS

To summarize, we found that for bulk rubrene single crystals the momentum dependence of the singlet excitons is qualitatively similar to that of the valence and conduction bands of the electronic band structure. We found a significant bandwidth along Γ–Y and a smaller one along Γ–X, although both were smaller than those of both electronic bands. The triplet excitons on the other hand show much smaller bandwidths of just 0.05 eV along Γ–Y and virtually no bandwidth along Γ–X, compared to about 0.2 eV and less than 0.02 eV for the singlet excitons, respectively.

As the main reason for this difference between singlets and triplets we identified the **k**-point distributions of the transitions contributing to the excitons. Singlet excitons were mainly located at and around Γ, whereas triplet excitons were spread over the whole Brillouin zone.

Concomitantly triplet excitons are much more strongly localized in real space and nearly confined to a single molecule ("Frenkel excitons"), whereas singlet excitons include hopping to neighbors and are much more delocalized ("Wannier excitons").

For the thin film geometry, we found exciton energies that were generally similar to the bulk ones, even though the quasiparticle band gap was about 0.4 eV larger. Here the increased quasiparticle energy difference seems to be counteracted by the similarly increased electron-hole interaction.

ACKNOWLEDGMENT

We thank F. C. Bocquet and F. S. Tautz for fruitful discussions.

[1] J. Takeya, M. Yamagishi, Y. Tominari, R. Hirahara, Y. Nakazawa, T. Nishikawa, T. Kawase, T. Shimoda, and S. Ogawa, Very high-mobility organic single-crystal transistors with in-crystal conduction channels, Appl. Phys. Lett. **90**, 102120 (2007).

[2] A. Saeki, S. Seki, T. Takenobu, Y. Iwasa, and S. Tagawa, Mobility and dynamics of charge carriers in rubrene single crystals studied by flash-photolysis microwave conductivity and optical spectroscopy, Adv. Mater. **20**, 920 (2008).

[3] M.-M. Ling, C. Reese, A. L. Briseno, and Z. Bao, Non-destructive probing of the anisotropy of field-effect mobility in the rubrene single crystal, Synth. Met. **157**, 257 (2007).

[4] V. C. Sundar, J. Zaumseil, V. Podzorov, E. Menard, R. L. Willett, T. Someya, M. E. Gershenson, and J. A. Rogers, Elastomeric transistor stamps: Reversible probing of charge transport in organic crystals, Science **303**, 1644 (2004).

[5] V. Podzorov, E. Menard, A. Borissov, V. Kiryukhin, J. A. Rogers, and M. E. Gershenson, Intrinsic Charge Transport on the Surface of Organic Semiconductors, Phys. Rev. Lett. **93**, 086602 (2004).

[6] V. Podzorov, E. Menard, J. A. Rogers, and M. E. Gershenson, Hall Effect in the Accumulation Layers on the Surface of Organic Semiconductors, Phys. Rev. Lett. **95**, 226601 (2005).

[7] J. Takeya, K. Tsukagoshi, Y. Aoyagi, T. Takenobu, and Y. Iwasa, Hall effect of quasi-hole gas in organic single-crystal transistors, Jpn. J. Appl. Phys. **44**, L1393 (2005).

[8] S. I. Machida, Y. Nakayama, S. Duhm, Q. Xin, A. Funakoshi, N. Ogawa, S. Kera, N. Ueno, and H. Ishii, Highest-Occupied-Molecular-Orbital Band Dispersion of Rubrene Single Crystals as Observed by Angle-Resolved Ultraviolet Photoelectron Spectroscopy, Phys. Rev. Lett. **104**, 156401 (2010).

[9] Y. Nakayama, Y. Uragami, S. Machida, K. R. Koswattage, D. Yoshimura, H. Setoyama, T. Okajima, K. Mase, and H. Ishii, Full picture of valence band structure of rubrene single crystals probed by angle-resolved and excitation-energy-dependent photoelectron spectroscopy, Appl. Phys. Express **5**, 111601 (2012).

[10] S. Yanagisawa, Y. Morikawa, and A. Schindlmayr, HOMO band dispersion of crystalline rubrene: Effects of self-energy corrections within the *GW* approximation, Phys. Rev. B **88**, 115438 (2013).

[11] Z. Q. Li, V. Podzorov, N. Sai, M. C. Martin, M. E. Gershenson, M. Di Ventra, and D. N. Basov, Light Quasiparticles Dominate Electronic Transport in Molecular Crystal Field-Effect Transistors, Phys. Rev. Lett. **99**, 016403 (2007).

[12] Z. Wang, H. Okada, and S. Naka, Evaluation of reliability in rubrene-based organic light emitting devices with a mixed single layer, Jpn. J. Appl. Phys. **49**, 01AA02 (2010).

[13] Q. Chen, W. Jia, L. Chen, D. Yuan, Y. Zou, and Z. Xiong, Determining the origin of half-bandgap-voltage electroluminescence in bifunctional Rubrene/C60 devices, Sci. Rep. **6**, 25331 (2016).

[14] X. Tang, Y. Hu, W. Jia, R. Pan, J. Deng, J. Deng, Z. He, and Z. Xiong, Intersystem crossing and triplet fusion in singlet-fission-dominated rubrene-based OLEDs under high bias current, ACS Appl. Mater. Interfaces **10**, 1948 (2018).

[15] A. K. Pandey and J.-M. Nunzi, Rubrene/fullerene heterostructures with a half-gap electroluminescence threshold and large photovoltage, Adv. Mater. **19**, 3613 (2007).

[16] B. Verreet, P. Heremans, A. Stesmans, and B. P. Rand, Microcrystalline organic thin-film solar cells, Adv. Mater. **25**, 5504 (2013).

[17] N. Sai, M. L. Tiago, J. R. Chelikowsky, and F. A. Reboredo, Optical spectra and exchange-correlation effects in molecular crystals, Phys. Rev. B **77**, 161306(R) (2008).

[18] S. Tavazzi, A. Borghesi, A. Papagni, P. Spearman, L. Silvestri, A. Yassar, A. Camposeo, M. Polo, and D. Pisignano, Optical response and emission waveguiding in rubrene crystals, Phys. Rev. B **75**, 245416 (2007).

[19] P. Irkhin, A. Ryasnyanskiy, M. Koehler, and I. Biaggio, Absorption and photoluminescence spectroscopy of rubrene single crystals, Phys. Rev. B **86**, 085143 (2012).

[20] S. Sharifzadeh, A. Biller, L. Kronik, and J. B. Neaton, Quasiparticle and optical spectroscopy of the organic semiconductors pentacene and PTCDA from first principles, Phys. Rev. B **85**, 125307 (2012).

[21] P. Cudazzo, M. Gatti, and A. Rubio, Excitons in molecular crystals from first-principles many-body perturbation theory: Picene versus pentacene, Phys. Rev. B **86**, 195307 (2012).

[22] M. J. van Setten, F. Caruso, S. Sharifzadeh, X. Ren, M. Scheffler, F. Liu, J. Lischner, L. Lin, J. R. Deslippe, S. G. Louie, C. Yang, F. Weigend, J. B. Neaton, F. Evers, and P. Rinke, *GW* 100: Benchmarking G_0W_0 for molecular systems, J. Chem. Theory Comput. **11**, 5665 (2015).

[23] C. Faber, I. Duchemin, T. Deutsch, C. Attaccalite, V. Olevano, and X. Blase, Electron-phonon coupling and charge-transfer excitations in organic systems from many-body perturbation theory, J. Mater. Sci. **47**, 7472 (2012).

[24] D. Jacquemin, I. Duchemin, and X. Blase, Benchmarking the Bethe-Salpeter formalism on a standard organic molecular set, J. Chem. Theory Comput. **11**, 3290 (2015).

[25] F. Bruneval, S. M. Hamed, and J. B. Neaton, A systematic benchmark of the *ab initio* Bethe-Salpeter equation approach for low-lying optical excitations of small organic molecules, J. Chem. Phys. **142**, 244101 (2015).

[26] G. Samsonidze, F. J. Ribeiro, M. L. Cohen, and S. G. Louie, Quasiparticle and optical properties of polythiophene-derived polymers, Phys. Rev. B **90**, 035123 (2014).

[27] M. Gatti and F. Sottile, Exciton dispersion from first principles, Phys. Rev. B **88**, 155113 (2013).

[28] P. Cudazzo, M. Gatti, A. Rubio, and F. Sottile, Frenkel versus charge-transfer exciton dispersion in molecular crystals, Phys. Rev. B **88**, 195152 (2013).

[29] P. Cudazzo, F. Sottile, A. Rubio, and M. Gatti, Exciton dispersion in molecular solids, J. Phys.: Condens. Matter **27**, 113204 (2015).

[30] T. Deilmann and K. S. Thygesen, Finite-momentum exciton landscape in mono- and bilayer transition metal dichalcogenides, 2D Mater. **6**, 035003 (2019).

[31] C. Vorwerk, B. Aurich, C. Cocchi, and C. Draxl, Bethe–Salpeter equation for absorption and scattering spectroscopy: Implementation in the exciting code, Electron. Struct. **1**, 037001 (2019).

[32] M. Rohlfing and S. G. Louie, Electron-hole excitations and optical spectra from first principles, Phys. Rev. B **62**, 4927 (2000).

[33] T. Lettmann and M. Rohlfing, Electronic excitations of polythiophene within many-body perturbation theory with and without the Tamm–Dancoff approximation, J. Chem. Theory Comput. **15**, 4547 (2019).

[34] B. Baumeier, D. Andrienko, Y. Ma, and M. Rohlfing, Excited states of dicyanovinyl-substituted oligothiophenes from many-body green's functions theory, J. Chem. Theory Comput. **8**, 997 (2012).

[35] Y. Ma, M. Rohlfing, and C. Molteni, Excited states of biological chromophores studied using many-body perturbation theory: Effects of resonant-antiresonant coupling and dynamical screening, Phys. Rev. B **80**, 241405(R) (2009).

[36] Y. Ma, M. Rohlfing, and C. Molteni, Modeling the excited states of biological chromophores within many-body green's function theory, J. Chem. Theory Comput. **6**, 257 (2010).

[37] M. Grüning, A. Marini, and X. Gonze, Exciton-plasmon states in nanoscale materials: breakdown of the tamm-dancoff approximation, Nano Lett. **9**, 2820 (2009).

[38] P. Puschnig, C. Meisenbichler, and C. Ambrosch-Draxl, Excited state properties of organic semiconductors: Breakdown of the Tamm-Dancoff approximation, arXiv:1306.3790v2 (2013).

[39] O. D. Jurchescu, A. Meetsma, and T. T. M. Palstra, Low-temperature structure of rubrene single crystals grown by vapor transport, Acta Crystallogr. Sect. B **62**, 330 (2006).

[40] D. R. Hamann, Generalized norm-conserving pseudopotentials, Phys. Rev. B **40**, 2980 (1989).

[41] L. Kleinman and D. M. Bylander, Efficacious Form for Model Pseudopotentials, Phys. Rev. Lett. **48**, 1425 (1982).

[42] J. Wieferink, P. Krüger, and J. Pollmann, Improved hybrid algorithm with Gaussian basis sets and plane waves: First-principles calculations of ethylene adsorption on $\beta-$SiC(001)$-(3\times 2)$, Phys. Rev. B **74**, 205311 (2006).

[43] H. J. Monkhorst and J. D. Pack, Special points for Brillouin-zone integrations, Phys. Rev. B **13**, 5188 (1976).

[44] W. von der Linden and P. Horsch, Precise quasiparticle energies and Hartree-Fock bands of semiconductors and insulators, Phys. Rev. B **37**, 8351 (1988).

[45] M. Rohlfing, P. Krüger, and J. Pollmann, Efficient scheme for GW quasiparticle band-structure calculations with applications to bulk Si and to the Si(001)-(2×1) surface, Phys. Rev. B **52**, 1905 (1995).

[46] M. Rohlfing and S. G. Louie, Excitonic Effects and the Optical Absorption Spectrum of Hydrogenated Si Clusters, Phys. Rev. Lett. **80**, 3320 (1998).

[47] J. A. Berger, L. Reining, and F. Sottile, Efficient *GW* calculations for SnO_2, ZnO, and rubrene: The effective-energy technique, Phys. Rev. B **85**, 085126 (2012).

[48] K. S. Thygesen and A. Rubio, Renormalization of Molecular Quasiparticle Levels at Metal-Molecule Interfaces: Trends across Binding Regimes, Phys. Rev. Lett. **102**, 046802 (2009).

[49] M. Rohlfing, Redshift of Excitons in Carbon Nanotubes Caused by the Environment Polarizability, Phys. Rev. Lett. **108**, 087402 (2012).

[50] M. Drüppel, T. Deilmann, P. Krüger, and M. Rohlfing, Diversity of trion states and substrate effects in the optical properties of an MoS_2 monolayer, Nat. Commun. **8**, 2117 (2017).

[51] Y. Niu, S. Gonzalez-Abad, R. Frisenda, P. Marauhn, M. Drüppel, P. Gant, R. Schmidt, N. S. Taghavi, D. Barcons, A. J. Molina-Mendoza, S. Michaelis De Vasconcellos, R. Bratschitsch, D. Perez De Lara, M. Rohlfing, and A. Castellanos-Gomez, Thickness-dependent differential reflectance spectra of monolayer and few-layer MoS_2, $MoSe_2$, WS_2 and WSe_2, Nanomaterials **8**, 725 (2018).